

# Molecular-Beam Epitaxy of Two-Dimensional $\text{In}_2\text{Se}_3$ and Its Giant Electroresistance Switching in Ferroresistive Memory Junction

Sock Mui Poh,<sup>O,†,‡,ID</sup> Sherman Jun Rong Tan,<sup>O,†,‡,ID</sup> Han Wang,<sup>§</sup> Peng Song,<sup>‡,||</sup> Irfan H. Abidi,<sup>⊥</sup> Xiaoxu Zhao,<sup>†,‡,ID</sup> Jiadong Dan,<sup>†,§</sup> Jingsheng Chen,<sup>§,ID</sup> Zhengtang Luo,<sup>⊥,ID</sup> Stephen J. Pennycook,<sup>†,§,||</sup> Antonio H. Castro Neto,<sup>||,#</sup> and Kian Ping Loh<sup>\*,†,‡,||,ID</sup>

<sup>†</sup>NUS Graduate School for Integrative Sciences and Engineering, Centre for Life Sciences No. 05-01, 28 Medical Drive, 117456 Singapore

<sup>‡</sup>Department of Chemistry, National University of Singapore, Science Drive 3, 117543 Singapore

<sup>§</sup>Department of Materials Science and Engineering, National University of Singapore, 117575 Singapore

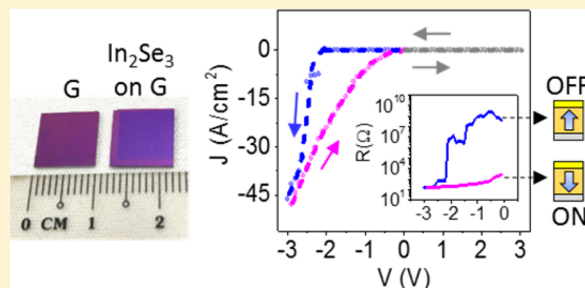
<sup>||</sup>Centre for Advanced 2D Materials and Graphene Research Centre, National University of Singapore, 117546 Singapore

<sup>⊥</sup>Department of Chemical and Biological Engineering, The Hong Kong University of Science and Technology, Clear Water Bay, Kowloon, Hong Kong

<sup>\*</sup>Department of Physics, National University of Singapore, 3 Science Drive 2, 117542 Singapore

## Supporting Information

**ABSTRACT:** Ferroelectric thin film has attracted great interest for nonvolatile memory applications and can be used in either ferroelectric Schottky diodes or ferroelectric tunneling junctions due to its promise of fast switching speed, high on-to-off ratio, and nondestructive readout. Two-dimensional  $\alpha$ -phase indium selenide ( $\text{In}_2\text{Se}_3$ ), which has a modest band gap and robust ferroelectric properties stabilized by dipole locking, is an excellent candidate for multidirectional piezoelectric and switchable photodiode applications. However, the large-scale synthesis of this material is still elusive, and its performance as a ferroresistive memory junction is rarely reported. Here, we report the low-temperature molecular-beam epitaxy (MBE) of large-area monolayer  $\alpha$ - $\text{In}_2\text{Se}_3$  on graphene and demonstrate the use of  $\alpha$ - $\text{In}_2\text{Se}_3$  on graphene in ferroelectric Schottky diode junctions by employing high-work-function gold as the top electrode. The polarization-modulated Schottky barrier formed at the interface exhibits a giant electroresistance ratio of  $3.9 \times 10^6$  with a readout current density of  $>12 \text{ A/cm}^2$ , which is more than 200% higher than the state-of-the-art technology. Our MBE growth method allows a high-quality ultrathin film of  $\text{In}_2\text{Se}_3$  to be heteroepitaxially grown on graphene, thereby simplifying the fabrication of high-performance 2D ferroelectric junctions for ferroresistive memory applications.



**KEYWORDS:**  $\text{In}_2\text{Se}_3$ , two-dimensional materials, molecular-beam epitaxy, ferroelectric Schottky diode, ferroresistive memory junction, giant electroresistance ratio

Ferroelectric Schottky diodes (FSDs) with polarization-modulated Schottky barriers are promising for applications in resistive switching memories, but its performance in terms of its on-to-off ratio and readout current densities are much poorer than ferroelectric tunneling junctions (FTJ).<sup>1,2</sup> This is because the insulating properties of oxide-based ferroelectric materials limit the maximum diode current, which precludes the stable detection of memory status using sense amplifiers, especially in miniaturized circuit elements.<sup>1</sup> Using thinner materials to improve current density, however, compromises the ferroelectric properties due to the presence of depolarization field, which strongly suppresses spontaneous polarization in thin materials.<sup>3</sup> The ideal ferroelectric material should, therefore, possess a modest band gap and also the ability to retain spontaneous out-of-plane polarization when scaled down to the

ultrathin level. Recently, 2D indium selenide ( $\alpha$ - $\text{In}_2\text{Se}_3$ ) was reported to exhibit spontaneous electric polarization.<sup>4–6</sup> Its unique noncentrosymmetric crystal structure leads to an intrinsic stabilization of in-plane and out-of-plane polarizations through dipole-locking,<sup>7</sup> giving rise to multidirectional piezoelectricity for applications such as electronic skin and energy-harvesting cells<sup>4,6</sup> as well as ferroelectricity for switchable diode devices.<sup>5</sup> The ferroelectric properties of  $\text{In}_2\text{Se}_3$  may provide additional control in applications of optoelectronics,<sup>8–10</sup> photovoltaics,<sup>11–13</sup> and thermoelectrics.<sup>14</sup> To harness its interesting optical and electronic properties, the large-scale

**Received:** July 2, 2018

**Revised:** September 6, 2018

**Published:** September 7, 2018

synthesis of ultrathin, high-quality  $\alpha$ -In<sub>2</sub>Se<sub>3</sub> is needed. To date, only isolated micrometer-sized  $\alpha$ -In<sub>2</sub>Se<sub>3</sub> crystals had been grown using chemical vapor deposition (CVD)<sup>5,15</sup> and physical vapor deposition (PVD)<sup>4,16,17</sup> approaches. The MBE growth of In<sub>2</sub>Se<sub>3</sub> has mostly been reported for thick film<sup>18–21</sup> using indium elemental sources, which is incompatible with the growth of ultrathin films due to its low melting point.

Herein, we report the molecular-beam epitaxy of continuous, centimeter-sized monolayer  $\alpha$ -In<sub>2</sub>Se<sub>3</sub> on single-layer graphene using the twin evaporation of In<sub>2</sub>Se<sub>3</sub> and Se precursors. The optimized growth temperature of 250 °C presents process advantages because it is significantly lower than CVD and PVD growth temperatures, which are typically >600 °C. Our growth method is highly versatile, and the conditions can be tuned to grow monolayer  $\alpha$ -In<sub>2</sub>Se<sub>3</sub>,  $\gamma$ -In<sub>2</sub>Se<sub>3</sub>, or InSe. Piezoresponse force microscopy (PFM) was used to characterize the ferroelectric properties of as-grown  $\alpha$ -In<sub>2</sub>Se<sub>3</sub> film of ~6 nm thickness with coercive voltages observed at +0.5 and -2.5 V. A MBE-grown few-layer  $\alpha$ -In<sub>2</sub>Se<sub>3</sub>-on-graphene structure was readily fabricated into a ferroresistive Schottky diode by using gold as the top electrode, achieving a giant electroresistance with an on-to-off ratio of up to  $3.9 \times 10^6$ , which is comparable with the state-of-the-art FTJs.<sup>22–24</sup> The current density obtained at the reading voltage of -1.4 V is at least 12 A/cm<sup>2</sup>, which is sufficient for detection by sense amplifier, even when miniaturized. The on-to-off ratio and readout current density are one of the highest values reported for FSDs,<sup>1,25,26</sup> and unlike FTJs, the fabricated In<sub>2</sub>Se<sub>3</sub> ferroelectric junction does not need additional engineering of interface barrier material.<sup>23,24,27</sup>

Monolayer indium selenide was epitaxially grown on single-layer graphene substrate at 250 °C using powdered In<sub>2</sub>Se<sub>3</sub> and Se precursors, as shown schematically in Figure 1a. To obtain high-quality  $\alpha$ -In<sub>2</sub>Se<sub>3</sub> film, a high flux ratio of Se/In<sub>2</sub>Se<sub>3</sub> ≈ 6:1 is needed. Keeping all other growth parameters constant, when only In<sub>2</sub>Se<sub>3</sub> is evaporated, monolayer InSe is grown instead (Figure S1). This can be attributed to the decomposition of In<sub>2</sub>Se<sub>3</sub> in Se-deficient environment.<sup>28</sup> The phases of the grown films were unambiguously determined by Raman spectroscopy.<sup>29,30</sup> For the film grown without Se precursor, four peaks are observed at ~116, 178, 200, and 227 cm<sup>-1</sup> (Figure 1b), which can be assigned to the A<sub>1</sub>, E, A<sub>1</sub>(LO), and A<sub>1</sub> Raman peaks of InSe, respectively.<sup>31</sup> When the film was grown with the coevaporation of In<sub>2</sub>Se<sub>3</sub> and Se precursors, pure-phase  $\alpha$ -In<sub>2</sub>Se<sub>3</sub> could be grown, as judged by the presence of the A<sub>1</sub>(LO + TO), A<sub>1</sub>(TO), and A<sub>1</sub>(LO) Raman signature peaks of  $\alpha$ -In<sub>2</sub>Se<sub>3</sub><sup>32,33</sup> at ~108, 176, and 205 cm<sup>-1</sup>, respectively (Figure 1d). We also investigated the growth condition of Se/In<sub>2</sub>Se<sub>3</sub> ≈ 3:1 and obtained the Raman spectrum dominated by peaks associated with InSe but with an extra peak at ~208 cm<sup>-1</sup> (black arrow, Figure 1c), which most likely originated from  $\alpha$ -In<sub>2</sub>Se<sub>3</sub>.

The morphology of the films grown under different conditions was analyzed using atomic force microscopy (AFM). In contrast to InSe (Figure 1e), the nucleation density of  $\alpha$ -In<sub>2</sub>Se<sub>3</sub> is much lower and its grains are much larger, better-faceted, and highly oriented (Figure 1g). However, the AFM of the mixed-phase indium selenide (Figure 1f) shows a similar grain size to that of pure InSe; it is notable that there is buckling of grain boundaries, which may be due to lateral lattice mismatch of InSe and  $\alpha$ -In<sub>2</sub>Se<sub>3</sub>. Such mixed-phase 2D materials can be developed for interesting electronic, chemical, and optical applications.<sup>34–36</sup>

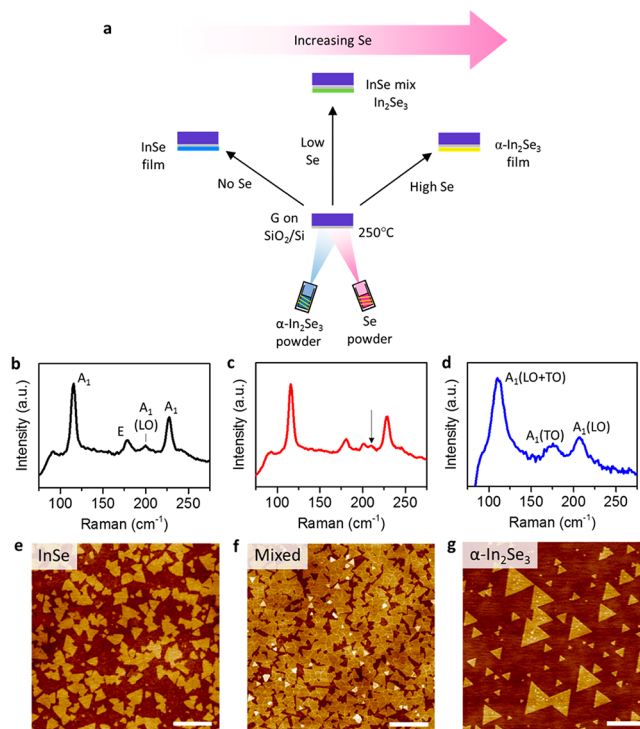


**Figure 1.** Controlled MBE growth of InSe to In<sub>2</sub>Se<sub>3</sub>. (a) Schematic illustration of the different growth conditions required to selectively grow the different binary phases of indium selenide. Raman of the (b) InSe grown under condition of only In<sub>2</sub>Se<sub>3</sub> precursor, (c) mixed InSe-In<sub>2</sub>Se<sub>3</sub> grown with precursor ratio Se/In<sub>2</sub>Se<sub>3</sub> = 3:1, and (d) In<sub>2</sub>Se<sub>3</sub> grown with precursor ratio Se/In<sub>2</sub>Se<sub>3</sub> = 6:1. AFM topography of the as-grown (e) InSe, (f) mixed InSe-In<sub>2</sub>Se<sub>3</sub>, and (g) In<sub>2</sub>Se<sub>3</sub>. Scale bars: 400 nm.

The growth mechanism of the  $\alpha$ -In<sub>2</sub>Se<sub>3</sub> films followed the Frank-van der Merwe growth mode,<sup>37,38</sup> in which lateral growth occurs much faster than vertical growth. We found that the optimum MBE growth of  $\alpha$ -In<sub>2</sub>Se<sub>3</sub> occurs at 250 °C because further increase in growth temperature results in a high desorption rate of grown In<sub>2</sub>Se<sub>3</sub> film (Figure S2). The growth of  $\alpha$ -In<sub>2</sub>Se<sub>3</sub> at this temperature is sufficient for the grains to coalesce and form continuous monolayer film (Figure 2a–c) with a growth rate of one monolayer in 2 h, which is much faster than the reported >10 h/ML MBE growth rate of monolayer transition metal dichalcogenides (TMDCs).<sup>39,40</sup> We noted that the monolayer  $\alpha$ -In<sub>2</sub>Se<sub>3</sub> is easily damaged under voltage-biased AFM tip or laser illumination due to its low thermal conductivity<sup>41</sup> and have exploited this property for the precise nanoscale etching and patterning of the ultrathin film<sup>42,43</sup> without the use of any mask or complicated lithography procedure (Figure 2d). The rectangular pattern was etched in the 4 nm thick  $\alpha$ -In<sub>2</sub>Se<sub>3</sub> with a 10 V biased AFM tip.

Other than studying growth parameters such as substrate temperature and precursor flux ratio, we also investigated the effect of substrate on the phase of the as-grown material, which is especially relevant for In<sub>2</sub>Se<sub>3</sub> due to its rich polymorphism. AFM topographic scans show that the grains grown on the epitaxial graphene substrate are well-aligned with 60° orientation. For controlled experiment, we performed the same growth on nonepitaxial SiO<sub>2</sub>/Si substrate, a commonly used substrate for CVD growth of single crystal TMDC.<sup>44</sup> A nonlayered growth morphology (Figure 2e) due to the growth of  $\gamma$ -In<sub>2</sub>Se<sub>3</sub><sup>33</sup> was obtained, as verified by the Raman signature peaks of this phase

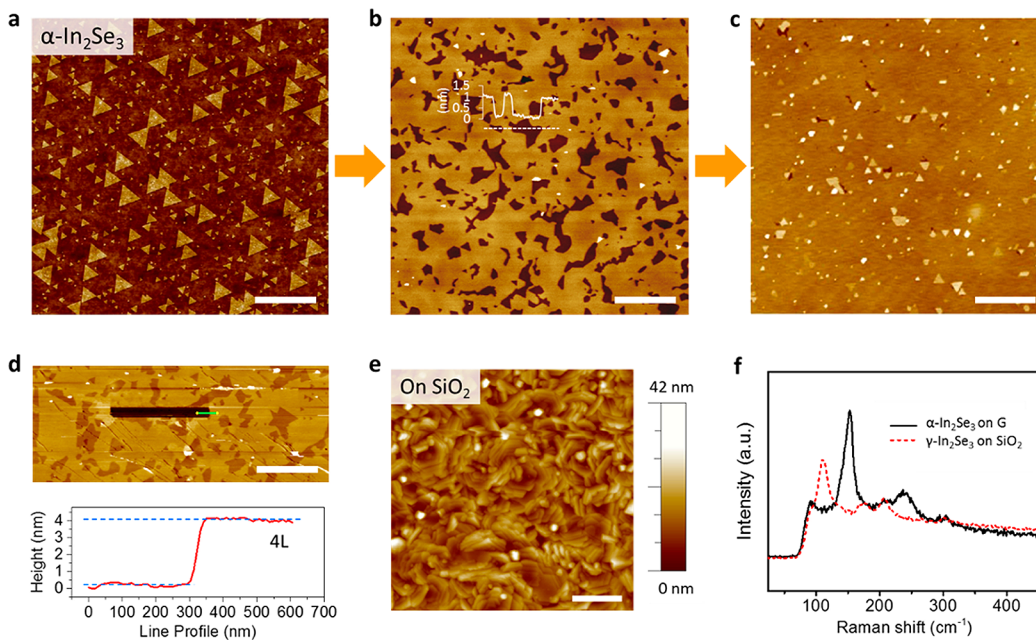


**Figure 2.** AFM characterization of MBE grown  $\alpha$ -In<sub>2</sub>Se<sub>3</sub> and  $\gamma$ -In<sub>2</sub>Se<sub>3</sub>. AFM topography showing the evolution in  $\alpha$ -In<sub>2</sub>Se<sub>3</sub> morphology as the growth progresses from (a) isolated facets to (b) coalescence and to (c) forming a continuous monolayer. (d) Etched hole of area of  $3\ \mu\text{m} \times 300\ \text{nm}$  on the as-grown 4 nm thick  $\alpha$ -In<sub>2</sub>Se<sub>3</sub> by 10 V-biased AFM contact tip. The bottom plot shows the corresponding height profile. (e) AFM topography of the  $\gamma$ -In<sub>2</sub>Se<sub>3</sub> grown on SiO<sub>2</sub>/Si substrate and its (f) corresponding Raman spectrum compared to that of  $\alpha$ -In<sub>2</sub>Se<sub>3</sub> grown on graphene. Scale bars: (a–c) 1  $\mu\text{m}$ , (d) 2  $\mu\text{m}$ , and (e) 400 nm.

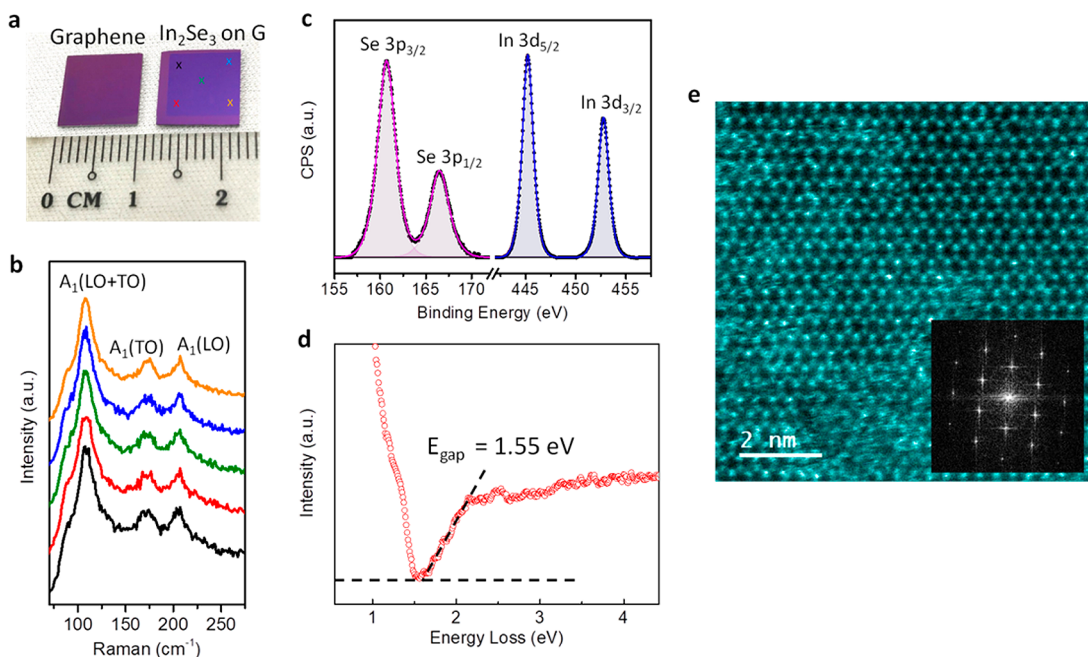


**Figure 3.** Large-area MBE growth of  $\alpha$ -In<sub>2</sub>Se<sub>3</sub> and its spectroscopic and microscopic characterizations. (a) Photograph of the 1  $\text{cm}^2$  graphene on SiO<sub>2</sub>/Si substrate and  $\sim 1\ \text{cm}^2$  MBE grown  $\alpha$ -In<sub>2</sub>Se<sub>3</sub> on the graphene/SiO<sub>2</sub>/Si substrate. (b) Raman spectra of the respective colored spots from the MBE-grown 1  $\text{cm}^2$  In<sub>2</sub>Se<sub>3</sub> shown in panel a. (c) XPS of the In 3d and Se 3p core orbital peaks of the grown  $\alpha$ -In<sub>2</sub>Se<sub>3</sub> film. (d) HREELS measured at specular angle of the grown  $\alpha$ -In<sub>2</sub>Se<sub>3</sub> film. The onset indicates the electronic bandgap. (e) STEM-ADF image of the grown  $\alpha$ -In<sub>2</sub>Se<sub>3</sub> monolayer. The inset shows the corresponding fast Fourier transform image.

at 152, 209, and 237  $\text{cm}^{-1}$  (Figure 2f). This shows that for the MBE growth of van der Waals 2D film, a substrate with matching crystal symmetry is required, in agreement with previous MBE studies of 2D transition-metal dichalcogenides.<sup>38,45</sup>

The MBE growth of  $\alpha$ -In<sub>2</sub>Se<sub>3</sub> film is highly scalable, and we demonstrate it on a 1  $\text{cm}^2$  CVD graphene layer on SiO<sub>2</sub>/Si,

prepared by the method described in ref 46 (Figure 3a). Raman spectra recorded from random spots on the grown sample are almost identical, attesting to the uniformity of the grown film (Figure 3b). X-ray photoemission spectroscopy (XPS) was used to probe the elemental composition and oxidation states of the grown film, as shown in Figure 3c. The spectra exhibit two

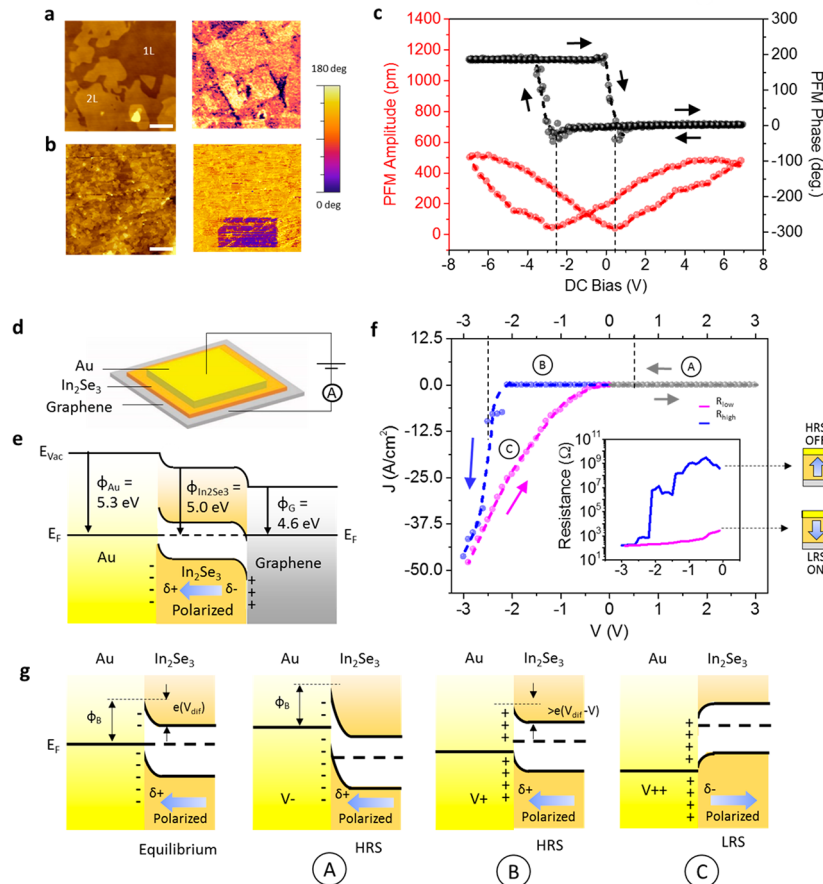


**Figure 4.** Ferroelectric properties and ferroresistive memory device performance of MBE-grown  $\alpha$ -In<sub>2</sub>Se<sub>3</sub>. (a) Topography and the corresponding PFM-phase image of the as-grown  $\alpha$ -In<sub>2</sub>Se<sub>3</sub>. Scale bar: 1  $\mu$ m. (b) Topography and the corresponding poled PFM-phase image. An area of  $5.2 \times 2.5 \mu\text{m}^2$  is poled by a  $-6$  V biased tip. Scale bar: 2  $\mu$ m. (c) Local PFM hysteresis curves of the as-grown film. (d) Schematics of the asymmetric ferroelectric memory junction fabricated on the as-grown 6 nm  $\alpha$ -In<sub>2</sub>Se<sub>3</sub> and its (e) corresponding band diagram alignments at equilibrium. (f)  $J(V)$  curve measured from the ferroelectric memory junction with respect to the graphene electrode. The inset shows the corresponding resistance of the blue (0 to  $-3$  V) and pink ( $-3$  to 0 V) curves. (g) Schematics showing the band diagram changes when voltage is applied, in correspondence to the marked A, B, and C regions of the (f)  $J(V)$  plot.

doublets with binding energies of 166.5, 160.7, 452.7, and 445.2 eV, which are assigned to the In<sub>2</sub>Se<sub>3</sub> XPS peaks for Se 3p<sub>1/2</sub>, Se 3p<sub>3/2</sub>, In 3d<sub>3/2</sub>, and In 3d<sub>5/2</sub> core level orbitals, respectively.<sup>47</sup> The elemental composition of In and Se was obtained by peak fitting with a mixed Gaussian–Lorentzian function after a Shirley background subtraction. XPS chemical composition analysis indicates an In-to-Se ratio of 2:3, confirming the presence of a pure In<sub>2</sub>Se<sub>3</sub> phase. There is very little surface oxidation because XPS only detected physisorbed oxygen (Figure S3).

The electronic band gap of the as-grown  $\alpha$ -In<sub>2</sub>Se<sub>3</sub> sample can be measured using high-resolution electron energy loss spectroscopy (HREELS). The energy-loss region was scanned in a specular geometry with incident electron energy of 16 eV, and the energy gap is determined from the sharp spectral onset delineated by an enhanced intensity from the background, which originates from interband electronic transitions.<sup>48,49</sup> As shown in Figure 3d, an energy onset of  $\sim 1.55$  eV was observed, which corresponds to the direct electronic bandgap of  $\alpha$ -In<sub>2</sub>Se<sub>3</sub>.<sup>50</sup> Scanning transmission electron microscopy-annular dark-field (STEM-ADF) image of the monolayer film (Figure 3e) shows a periodic hexagonal *P63/mmc* crystal lattice (Figure S4) with a lattice constant of 4.0 Å, which corresponds to the crystal structure of  $\alpha$ -In<sub>2</sub>Se<sub>3</sub>.<sup>51</sup> Therefore, both spectroscopic and

microscopic characterizations unambiguously identified the grown film as the  $\alpha$  phase of In<sub>2</sub>Se<sub>3</sub>.

The piezoelectric and ferroelectric properties of the MBE-grown  $\alpha$ -In<sub>2</sub>Se<sub>3</sub> were characterized using high-resolution PFM. Figure 4a shows the topography and the corresponding out-of-plane PFM-phase domains of the MBE-grown 1-2L In<sub>2</sub>Se<sub>3</sub>. The low contrast in the polarization of the PFM phase can be attributed to the small out-of-plane polarization.<sup>5</sup> Notably, the pristine PFM domains are distinct from the topography, indicating that the formation of domains did not arise purely due to topography differences or artifacts in measurement. Spontaneous polarization was induced by a DC bias of  $-6$  V, and a  $5.2 \mu\text{m} \times 2.5 \mu\text{m}$  domain was written on the  $\sim 6$  nm thick In<sub>2</sub>Se<sub>3</sub>, which evidence the ferroelectric nature of the film (Figure 4b). Using switching-spectroscopy PFM, a typical ferroelectric butterfly loop and hysteresis loop are observed for the PFM amplitude and PFM phase, respectively (Figure 4c). The measured coercive voltages are approximately  $+0.5$  and  $-2.5$  V.

Giant electroresistance ratio of at least  $10^4$  is highly desirable for ferroresistive memory device.<sup>2</sup> However, this is rarely observed in nontunneling ferroelectric diode devices.<sup>26</sup> The use of a 2D ferroelectric narrow-band-gap semiconductor allows better tuning of the Schottky barrier through enhancing the

Coulomb interactions from its reduced dielectric screening.<sup>52</sup> To further enlarge the differences between the “on”-state and the “off”-state resistance, an asymmetric electrode configuration can be used. To demonstrate such a device, a ferroelectric junction was fabricated on the MBE grown 6 nm film by evaporating gold (Au) electrode on top and using the graphene substrate directly as the bottom electrode, as shown in Figure 4d. The resultant band alignments are shown in Figure 4e. The measured  $J(V)$  characteristics with bias applied to the graphene electrode show a rectifying behavior and a strong hysteresis in the negative bias range (Figure 4f), in which a sharp increase of current density is observed at  $-2.5$  V. This value coincides with the switching voltage measured by PFM, which, therefore, indicates that the  $J(V)$  behavior is determined by the ferroelectric polarizations. The calculated resistance,  $R$ , equals voltage divided by current for the respective forward (blue, 0 V to  $-3$  V) and backward (pink,  $-3$  V to 0 V) measurements and is shown in the inset of Figure 4f. Remarkably, the ratio between the high-resistance state (HRS) and low-resistance state (LRS) is as high as  $3.9 \times 10^6$ , exhibiting a giant electroresistance ratio.<sup>22,53</sup> This device performance demonstrates that few-layer  $\text{In}_2\text{Se}_3$  ferroelectric semiconductor junction can be used as random access memory, requiring a low voltage of  $\pm 4$  V to write and approximately  $-1$  V to read. At the reading voltage of  $-1.4$  V, the current density is at least  $12 \text{ A/cm}^2$ , which is more than 200% higher than typical ferroelectric diode junctions.<sup>1,25</sup> Such high current density can be ascribed to the 2D van der Waals nature of  $\text{In}_2\text{Se}_3$ <sup>54</sup> and provides unambiguous differentiation of the “on” and “off” states for memory sense amplifiers.

It should be noted that  $\alpha\text{-In}_2\text{Se}_3$  grown on highly ordered pyrolytic graphite (HOPG) substrate gave the same performance as that grown on single layer graphene when fabricated as ferroelectric resistive memory device; thus, the thickness of graphene is not critical to the memory junction performance. The giant electroresistance switching effect can be explained by the interplay of two synergistic factors: (1) the use of 2D van der Waals ferroelectric semiconductor and (2) the use of highly asymmetric electrodes with higher and lower work function than the ferroelectric semiconductor. First, the use of a ferroelectric semiconductor enables the conductivity to be controlled by modulating the width and height of the Schottky barrier<sup>25,55</sup> via the polarization of the ferroelectric. Second, the asymmetric electrodes provide a high rectification ratio. Films thicker than 6 nm were used due to their higher thermal stability and resistance to electron beam-induced damage (Figure 2d). Due to work function differences (UPS of  $\text{In}_2\text{Se}_3$  in Figure S5), at the metal–semiconductor interfaces, electrons flow from graphene to  $\text{In}_2\text{Se}_3$  and from  $\text{In}_2\text{Se}_3$  to Au to form space-charged regions. The asymmetric space-charge interfaces thus result in an intrinsic preferential polarization state in the  $\text{In}_2\text{Se}_3$  film due to Coulomb interactions (Figure 4e). This also explains the asymmetric coercive voltages measured by PFM. Because  $\text{In}_2\text{Se}_3$  is an  $n$ -type semiconductor (Figure S5), the graphene– $\text{In}_2\text{Se}_3$  interface forms an injecting Ohmic contact, and the Au– $\text{In}_2\text{Se}_3$  interface forms a Schottky contact, with the potential barrier given as:<sup>56</sup>

$$\phi_B = \phi_M - \chi$$

where  $\phi_B$  is the Schottky barrier,  $\phi_M$  is the work function of metal, and  $\chi$  is the electron affinity of the semiconductor.  $\phi_B$  is calculated to be 1.7 eV based on the work function of Au as 5.3 eV, and the electron affinity of  $\text{In}_2\text{Se}_3$  was calculated as 3.6 eV.<sup>57</sup>

Figure 4g illustrates the changes in the Schottky barrier when a voltage bias is applied. At equilibrium, there exists a space-

charged depleted region, with a calculated Schottky barrier of  $\sim 1.7$  eV. When a negative bias is applied to the Au electrode (positive bias to graphene, as in the Figure 4f plot), the depletion zone width increases.<sup>56</sup> At a voltage bias greater than the coercive voltage (more positive than 0.5 V with respect to graphene), the polarization flips toward the Au electrode and reduces the diffusion potential of the depletion zone. However, the Schottky barrier seen by the transporting electrons does not reduce and electron flow is low (region A of Figure 4f plot). When a positive bias is applied at the Au electrode (the negative region in Figure 4f plot, with respect to graphene), the barrier seen by the electron flow is given by the diffusion potential:<sup>56</sup>

$$e(V_{\text{dif}}) = \phi_M - \phi_S$$

where  $e(V_{\text{dif}})$  is the diffusion potential and  $\phi_S$  is the work function of the semiconductor. It is calculated to be 0.3 eV. With applied bias  $V$ , the barrier is reduced by the amount  $e(V)$ . Because the applied bias still is below that of the coercive voltage for flipping (magnitude lower than  $-2.5$  V), the polarization in  $\text{In}_2\text{Se}_3$  still points toward the Au electrode and adds on to the potential barrier, making it slightly higher than  $e(V_{\text{dif}} - V)$ . As such, it is still in HRS as shown in region B of Figure 4f, and transport is characterized by Schottky emission,<sup>55</sup> with the relationship<sup>56</sup> (Figure S6):

$$I = I_0 \left[ \exp\left(\frac{eV}{kT}\right) - 1 \right]$$

When the magnitude of applied bias is more than the coercive field ( $-2.5$  V with respect to graphene), the polarization in  $\text{In}_2\text{Se}_3$  reverse and points toward the graphene electrode, resulting in the reversal of the band bending,<sup>22,23</sup> and the transport characteristics is ohmic (Figure S6). The lowest resistance is obtained (region C of Figure 4f) when the ferroelectric polarization direction is parallel to the built-in electric field at the metal–semiconductor interface.<sup>55</sup> It is noted that during discharge, there will be no changes to the injecting ohmic contact at graphene– $\text{In}_2\text{Se}_3$ ; applied bias is distributed across the semiconductor junction, and is not taken up in the contact area, unlike the Schottky contact.<sup>56</sup>

The use of graphene as the substrate serves two purposes. The first is as an epitaxial substrate for the growth of highly crystalline  $\text{In}_2\text{Se}_3$  films. Another role is to serve as a low-work-function electrode to compliment the high-work-function gold electrode; such an asymmetric electrode design maximizes the polarization effect. In view of the fact that the growth of CVD graphene by roll-to-roll process has entered the first stage of commercialization, the epitaxial growth of ultrathin  $\alpha\text{-In}_2\text{Se}_3$  on graphene by MBE provides convenient integration in the large-scale fabrication of ferroelectric junctions because high-work-function metal such as gold can be directly sputtered onto  $\alpha\text{-In}_2\text{Se}_3$ –graphene. Another important point is that no “transfer” is needed in this process because the ferroelectric material is directly grown on graphene. Furthermore, the advantage of using  $\alpha\text{-In}_2\text{Se}_3$  ferroelectric Schottky diode is that no additional engineering of the barrier is needed, unlike the case of FTJ. Highly competitive performances for on–off current and readout diode current can be achieved compared with FTJ and state-of-the-art ferroelectric diodes. The good performance of our ferroelectric junction may be related to the much lower growth temperature used in our MBE growth ( $250^\circ\text{C}$ ) as compared with CVD methods ( $>600^\circ\text{C}$ ) because high growth temperature can cause the desorption of highly volatile indium

or selenium species, leading to defects and interfacial traps, which affect reproducibility and stability of switchable diode behavior.<sup>58</sup>

In conclusion, we have developed a method to grow large area  $\alpha$ -In<sub>2</sub>Se<sub>3</sub> films on graphene by MBE, using In<sub>2</sub>Se<sub>3</sub> and Se powder precursors and at a low growth temperature of 250 °C. The epitaxial growth grains are highly crystalline and well-oriented, which coalesce to form a uniform and continuous monolayer of  $\alpha$ -In<sub>2</sub>Se<sub>3</sub>. Our MBE growth method can be readily controlled to grow pure phases of monolayer  $\alpha$ -In<sub>2</sub>Se<sub>3</sub>, InSe, and  $\gamma$ -In<sub>2</sub>Se<sub>3</sub> as well as mixed phases such as InSe–In<sub>2</sub>Se<sub>3</sub>. We further designed an asymmetric ferroresistive memory device to exploit the 2D semiconducting ferroelectric nature of  $\alpha$ -In<sub>2</sub>Se<sub>3</sub> and achieve outstanding performances, with giant electroresistance ratios of  $3.9 \times 10^6$  and readout current densities of  $>12$  A/cm<sup>2</sup>. The successful heteroepitaxial growth of large area ferroelectric semiconductor on graphene at modest growth temperatures allows the convenient fabrication of high-performance ferroelectric Schottky diodes for memory applications.

**MBE Growth of Samples.** Indium selenides were grown in a customized MBE chamber with a base pressure  $\sim 6 \times 10^{-10}$  Torr. Prior to growth, the substrate was degassed in an ultrahigh-vacuum chamber for 30 min and annealed at 600 °C for 5 min. Single-layer graphene on SiO<sub>2</sub>/Si is used as the substrate unless otherwise stated. Ultrapure In<sub>2</sub>Se<sub>3</sub> powder (99.99%) and Se pellets (99.999%) were evaporated from a crucible heated by an electron beam source and a hot-lip effusion cell, respectively. For the growth of In<sub>2</sub>Se<sub>3</sub>, the temperature of Se crucible cells was maintained at 150 °C with a hot-lip at 220 °C. The flux ratio of the precursors are as described in the main text. The chamber pressure during growth was  $\sim 1 \times 10^{-8}$  Torr when the selenium source is used and  $\sim 6 \times 10^{-9}$  Torr when only In<sub>2</sub>Se<sub>3</sub> is evaporated.

**Atomic Force Microscopy.** Atomic force microscopy was performed using Bruker Dimension FastScan Atomic Force Microscope in noncontact mode at room temperature. High-resolution PFM measurements were carried out with a commercial scanning probe microscope (Asylum Research MFP-3D) instrument at ambient atmosphere. Pt-coated tips (AC240TM, spring constant of  $\sim 2$  N m<sup>-1</sup>, Olympus, Japan) were used to measure the local switching spectrum and out-of-plane PFM image. The typical scan rate for all scan modes was 1 Hz. The drive frequency, drive amplitude ( $V_{AC}$ ), and trigger force were  $\sim 270$  kHz, 1 V, and 80 nN, respectively. To induce polarization in the ferroelectric material,  $-6$  V DC voltage was applied to the conductive tip onto the sample and the sample scanned via normal PFM measurements.

**Raman Spectroscopy.** Raman spectra were recorded at room temperature using the confocal WiTec Alpha 300R Raman Microscope with laser excitation at 532 nm and power of  $<100$   $\mu$ W.

**Scanning Transmission Electron Microscopy.** STEM-ADF imaging was performed using an aberration-corrected JEOL ARM200F, equipped with a cold field emission gun, operating at 80 kV.

**High-Resolution Electron Energy-Loss Spectroscopy.** HREELS measurements were performed using a Delta 0.5 spectrometer (SPECS, GmbH) with specular geometry in the coarse mode. The impinging electron energy is set to 16 eV with an energy resolution of 30 meV.

**X-ray and Ultraviolet Photoemission Spectroscopies.** XPS characterizations were performed using SPECS XR-50 X-ray Mg K $\alpha$  (1253.7 eV) source with a pass energy of 30 eV and a

spot size of 5 mm. Detection was done by a PHOIBOS 150 hemispherical energy analyzer (SPECS, GmbH). The binding energies of the XPS spectra were calibrated using Au 4f<sub>7/2</sub> peaks. XPS peak fitting was carried out using a mixed Gaussian–Lorentzian function after a Shirley background subtraction. Area ratios of 3:2 between the In 3d<sub>5/2</sub> and In 3d<sub>3/2</sub> and 2:1 between the Se 3p<sub>3/2</sub> and Se 3p<sub>1/2</sub> peaks were employed in the fit with same full width at half-maximum. UPS measurements were performed with monochromated photon energy of 21.2 eV (He I) and 40.8 eV (He II) through a toroidal mirror monochromator (SPECS GmbH). The detector used is the same as XPS characterizations. The experiments were performed in a chamber of base pressure greater than  $5 \times 10^{-10}$  mbar.

**Device Fabrication and Measurements.** Top gold electrodes with thicknesses of 50 nm were deposited via thermal evaporation directly on the  $\alpha$ -In<sub>2</sub>Se<sub>3</sub>–graphene samples using a copper grid mask of hole 200  $\mu$ m  $\times$  200  $\mu$ m. Electrical measurements were carried out at room temperature using Keithley 6430 SourceMeter to record  $J(V)$  curves (0  $\rightarrow$  +3.0 V  $\rightarrow$  -3.0 V  $\rightarrow$  0).

## ■ ASSOCIATED CONTENT

### S Supporting Information

The Supporting Information is available free of charge on the ACS Publications website at DOI: [10.1021/acs.nanolett.8b02688](https://doi.org/10.1021/acs.nanolett.8b02688).

Figures showing MBE growth, desorption of grown  $\alpha$ -In<sub>2</sub>Se<sub>3</sub>, XPS analysis, identification of the structural phase of  $\alpha$ -In<sub>2</sub>Se<sub>3</sub>, UPS of MBE-grown  $\alpha$ -In<sub>2</sub>Se<sub>3</sub>, and conduction mechanisms ([PDF](#))

## ■ AUTHOR INFORMATION

### Corresponding Author

\*E-mail: [chmlohkp@nus.edu.sg](mailto:chmlohkp@nus.edu.sg).

### ORCID

Sock Mui Poh: [0000-0002-6289-4519](https://orcid.org/0000-0002-6289-4519)

Sherman Jun Rong Tan: [0000-0003-1591-3497](https://orcid.org/0000-0003-1591-3497)

Xiaoxu Zhao: [0000-0001-9746-3770](https://orcid.org/0000-0001-9746-3770)

Jingsheng Chen: [0000-0003-3188-2803](https://orcid.org/0000-0003-3188-2803)

Zhengtang Luo: [0000-0002-4822-9694](https://orcid.org/0000-0002-4822-9694)

Kian Ping Loh: [0000-0002-1491-743X](https://orcid.org/0000-0002-1491-743X)

### Author Contributions

○S.M.P. and S.J.R.T. contributed equally. The manuscript was written through contributions of all authors. All authors have given approval to the final version of the manuscript.

### Funding

K.P.L. thanks the National Research Foundation, Prime's Minister Office, for support under the midsized Research Centre (CA2DM). We also acknowledge funding support from the Singapore National Research Foundation (NRF) through the Singapore Berkeley Research Initiative for Sustainable Energy (SinBeRISE) Programme.

### Notes

The authors declare no competing financial interest.

## ■ REFERENCES

- (1) Jeong, D. S.; Thomas, R.; Katiyar, R. S.; Scott, J. F.; Kohlstedt, H.; Petrucci, A.; Hwang, C. S. *Rep. Prog. Phys.* **2012**, *75*, 076502.
- (2) Garcia, V.; Bibes, M. *Nat. Commun.* **2014**, *5*, 4289.
- (3) Junquera, J.; Ghosez, P. *Nature* **2003**, *422*, 506.

- (4) Zhou, Y.; Wu, D.; Zhu, Y.; Cho, Y.; He, Q.; Yang, X.; Herrera, K.; Chu, Z.; Han, Y.; Downer, M. C.; Peng, H.; Lai, K. *Nano Lett.* **2017**, *17*, 5508–5513.
- (5) Cui, C.; Hu, W.-J.; Yan, X.; Addiego, C.; Gao, W.; Wang, Y.; Wang, Z.; Li, L.; Cheng, Y.; Li, P.; Zhang, X.; Alshareef, H. N.; Wu, T.; Zhu, W.; Pan, X.; Li, L.-J. *Nano Lett.* **2018**, *18*, 1253–1258.
- (6) Xue, F.; Zhang, J.; Hu, W.; Hsu, W.-T.; Han, A.; Leung, S.-F.; Huang, J.-K.; Wan, Y.; Liu, S.; Zhang, J.; He, J.-H.; Chang, W.-H.; Wang, Z. L.; Zhang, X.; Li, L.-J. *ACS Nano* **2018**, *12*, 4976–4983.
- (7) Xiao, J.; Zhu, H.; Wang, Y.; Feng, W.; Hu, Y.; Dasgupta, A.; Han, Y.; Wang, Y.; Muller, D. A.; Martin, L. W.; Hu, P.; Zhang, X. *Phys. Rev. Lett.* **2018**, *120*, 227601.
- (8) Jacobs-Gedrim, R. B.; Shanmugam, M.; Jain, N.; Durcan, C. A.; Murphy, M. T.; Murray, T. M.; Matyi, R. J.; Moore, R. L.; Yu, B. *ACS Nano* **2014**, *8*, 514–521.
- (9) Island, J. O.; Blanter, S. I.; Buscema, M.; van der Zant, H. S. J.; Castellanos-Gomez, A. *Nano Lett.* **2015**, *15*, 7853–7858.
- (10) Zhai, T.; Fang, X.; Liao, M.; Xu, X.; Li, L.; Liu, B.; Koide, Y.; Ma, Y.; Yao, J.; Bando, Y.; Golberg, D. *ACS Nano* **2010**, *4*, 1596–1602.
- (11) Kwon, S. H.; Ahn, B. T.; Kim, S. K.; Yoon, K. H.; Song, J. *Thin Solid Films* **1998**, *323*, 265–269.
- (12) Li, H.; Ren, W.; Gao, L.; Wang, G.; Peng, R.; Li, H.; Zhang, P.; Shafa, M.; Tong, X.; Luo, S.; et al. *J. Phys. D: Appl. Phys.* **2016**, *49*, 145108.
- (13) Park, S. C.; Lee, D. Y.; Ahn, B. T.; Yoon, K. H.; Song, J. *Sol. Energy Mater. Sol. Cells* **2001**, *69*, 99–105.
- (14) Han, G.; Chen, Z. G.; Drennan, J.; Zou, J. *Small* **2014**, *10*, 2747–2765.
- (15) Feng, W.; Zheng, W.; Gao, F.; Chen, X.; Liu, G.; Hasan, T.; Cao, W.; Hu, P. *Chem. Mater.* **2016**, *28*, 4278–4283.
- (16) Zhou, J.; Zeng, Q.; Lv, D.; Sun, L.; Niu, L.; Fu, W.; Liu, F.; Shen, Z.; Jin, C.; Liu, Z. *Nano Lett.* **2015**, *15*, 6400–6405.
- (17) Lin, M.; Wu, D.; Zhou, Y.; Huang, W.; Jiang, W.; Zheng, W.; Zhao, S.; Jin, C.; Guo, Y.; Peng, H.; Liu, Z. *J. Am. Chem. Soc.* **2013**, *135*, 13274–13277.
- (18) Okamoto, T.; Yamada, A.; Konagai, M. *J. Cryst. Growth* **1997**, *175–176*, 1045–1050.
- (19) Ohtsuka, T.; Okamoto, T.; Yamada, A.; Konagai, M. *Jpn. J. Appl. Phys.* **1999**, *38*, 668.
- (20) Ohtsuka, T.; Nakanishi, K.; Okamoto, T.; Yamada, A.; Konagai, M.; Jahn, U. *Jpn. J. Appl. Phys.* **2001**, *40*, 509.
- (21) Okamoto, T.; Nakada, Y.; Aoki, T.; Takaba, Y.; Yamada, A.; Konagai, M. *Phys. Status Solidi C* **2006**, *3*, 2796–2799.
- (22) Xi, Z.; Ruan, J.; Li, C.; Zheng, C.; Wen, Z.; Dai, J.; Li, A.; Wu, D. *Nat. Commun.* **2017**, *8*, 15217.
- (23) Wen, Z.; Li, C.; Wu, D.; Li, A.; Ming, N. *Nat. Mater.* **2013**, *12*, 617.
- (24) Yin, Y. W.; Burton, J. D.; Kim, Y. M.; Borisevich, A. Y.; Pennycook, S. J.; Yang, S. M.; Noh, T. W.; Gruverman, A.; Li, X. G.; Tsymbal, E. Y.; Li, Q. *Nat. Mater.* **2013**, *12*, 397.
- (25) Jiang, A. Q.; Wang, C.; Jin, K. J.; Liu, X. B.; Scott, J. F.; Hwang, C. S.; Tang, T. A.; Lu, H. B.; Yang, G. Z. *Adv. Mater.* **2011**, *23*, 1277–1281.
- (26) Hong, S.; Choi, T.; Jeon, J. H.; Kim, Y.; Lee, H.; Joo, H. Y.; Hwang, I.; Kim, J. S.; Kang, S. O.; Kalinin, S. V.; Park, B. H. *Adv. Mater.* **2013**, *25*, 2339–2343.
- (27) Wang, L.; Cho, M. R.; Shin, Y. J.; Kim, J. R.; Das, S.; Yoon, J.-G.; Chung, J.-S.; Noh, T. W. *Nano Lett.* **2016**, *16*, 3911–3918.
- (28) Wang, J.-J.; Cao, F.-F.; Jiang, L.; Guo, Y.-G.; Hu, W.-P.; Wan, L.-J. *J. Am. Chem. Soc.* **2009**, *131*, 15602–15603.
- (29) Ferrari, A. C. *Solid State Commun.* **2007**, *143*, 47–57.
- (30) Li, H.; Zhang, Q.; Yap, C. C. R.; Tay, B. K.; Edwin, T. H. T.; Olivier, A.; Baillargeat, D. *Adv. Funct. Mater.* **2012**, *22*, 1385–1390.
- (31) Lei, S.; Ge, L.; Najmaei, S.; George, A.; Kappera, R.; Lou, J.; Chhowalla, M.; Yamaguchi, H.; Gupta, G.; Vajtai, R.; Mohite, A. D.; Ajayan, P. M. *ACS Nano* **2014**, *8*, 1263–1272.
- (32) Chen, Y.-l.; Li, M.-l.; Wu, Y.-m.; Li, S.-j.; Lin, Y.; Du, D.-x.; Ding, H.-y.; Pan, N.; Wang, X.-p. *Chin. J. Chem. Phys.* **2017**, *30*, 325–332.
- (33) Kambas, K.; Julien, C.; Jouanne, M.; Likforman, A.; Guittard, M. *Phys. Status Solidi B* **1984**, *124*, K105–K108.
- (34) Kappera, R.; Voiry, D.; Yalcin, S. E.; Branch, B.; Gupta, G.; Mohite, A. D.; Chhowalla, M. *Nat. Mater.* **2014**, *13*, 1128.
- (35) Voiry, D.; Goswami, A.; Kappera, R.; Silva, C. d. C. C. e.; Kaplan, D.; Fujita, T.; Chen, M.; Asefa, T.; Chhowalla, M. *Nat. Chem.* **2015**, *7*, 45.
- (36) Tan, S. J. R.; Abdelwahab, I.; Ding, Z.; Zhao, X.; Yang, T.; Loke, G. Z. J.; Lin, H.; Verzhbitskiy, I.; Poh, S. M.; Xu, H.; Nai, C. T.; Zhou, W.; Eda, G.; Jia, B.; Loh, K. P. *J. Am. Chem. Soc.* **2017**, *139*, 2504–2511.
- (37) Venables, J. A.; Spiller, G. D. T.; Hanbucken, M. *Rep. Prog. Phys.* **1984**, *47*, 399.
- (38) Poh, S. M.; Zhao, X.; Tan, S. J. R.; Fu, D.; Fei, W.; Chu, L.; Jiadong, D.; Zhou, W.; Pennycook, S. J.; Castro Neto, A. H.; Loh, K. P. *ACS Nano* **2018**, *12*, 7562.
- (39) Fu, D.; Zhao, X.; Zhang, Y.-Y.; Li, L.; Xu, H.; Jang, A. R.; Yoon, S. I.; Song, P.; Poh, S. M.; Ren, T.; Ding, Z.; Fu, W.; Shin, T. J.; Shin, H. S.; Pantelides, S. T.; Zhou, W.; Loh, K. P. *J. Am. Chem. Soc.* **2017**, *139*, 9392–9400.
- (40) Kang, K.; Xie, S.; Huang, L.; Han, Y.; Huang, P. Y.; Mak, K. F.; Kim, C.-J.; Muller, D.; Park, J. *Nature* **2015**, *520*, 656.
- (41) Zhou, S.; Tao, X.; Gu, Y. J. *J. Phys. Chem. C* **2016**, *120*, 4753–4758.
- (42) Berger, C.; Song, Z.; Li, X.; Wu, X.; Brown, N.; Naud, C.; Mayou, D.; Li, T.; Hass, J.; Marchenkov, A. N.; Conrad, E. H.; First, P. N.; de Heer, W. A. *Science* **2006**, *312*, 1191.
- (43) Mahjouri-Samani, M.; Lin, M.-W.; Wang, K.; Lupini, A. R.; Lee, J.; Basile, L.; Boulesbaa, A.; Rouleau, C. M.; Puretzky, A. A.; Ivanov, I. N.; Xiao, K.; Yoon, M.; Geohegan, D. B. *Nat. Commun.* **2015**, *6*, 7749.
- (44) Gong, Y.; Ye, G.; Lei, S.; Shi, G.; He, Y.; Lin, J.; Zhang, X.; Vajtai, R.; Pantelides, S. T.; Zhou, W.; Li, B.; Ajayan, P. M. *Adv. Funct. Mater.* **2016**, *26*, 2009–2015.
- (45) Poh, S. M.; Tan, S. J. R.; Zhao, X.; Chen, Z.; Abdelwahab, I.; Fu, D.; Xu, H.; Bao, Y.; Zhou, W.; Loh, K. P. *Adv. Mater.* **2017**, *29*, 1605641.
- (46) Abidi Irfan, H.; Liu, Y.; Pan, J.; Tyagi, A.; Zhuang, M.; Zhang, Q.; Cagang Aldrine, A.; Weng, L. T.; Sheng, P.; Goddard William, A.; Luo, Z. *Adv. Funct. Mater.* **2017**, *27*, 1700121.
- (47) Zheng, Z. Q.; Yao, J. D.; Yang, G. W. *J. Mater. Chem. C* **2016**, *4*, 8094–8103.
- (48) Tan Sherman Jun, R.; Abdelwahab, I.; Chu, L.; Poh Sock, M.; Liu, Y.; Lu, J.; Chen, W.; Loh Kian, P. *Adv. Mater.* **2018**, *30*, 1704619.
- (49) Vos, M.; King, S. W.; French, B. L. *J. Electron Spectrosc. Relat. Phenom.* **2016**, *212*, 74–80.
- (50) Hu, L.; Huang, X. *RSC Adv.* **2017**, *7*, 55034–55043.
- (51) In<sub>2</sub>Se<sub>3</sub> crystal structure, phases. In *Ternary Compounds, Organic Semiconductors*; Madelung, O.; Rössler, U.; Schulz, M., Eds.; Springer Berlin Heidelberg: Berlin, Germany, 2000; pp 1–5.
- (52) Mak, K. F.; He, K.; Lee, C.; Lee, G. H.; Hone, J.; Heinz, T. F.; Shan, J. *Nat. Mater.* **2013**, *12*, 207.
- (53) Zhuravlev, M. Y.; Sabirianov, R. F.; Jaswal, S. S.; Tsymbal, E. Y. *Phys. Rev. Lett.* **2005**, *94*, 246802.
- (54) Lembke, D.; Kis, A. *ACS Nano* **2012**, *6*, 10070–10075.
- (55) Blom, P. W. M.; Wolf, R. M.; Cillessen, J. F. M.; Krijn, M. P. C. M. *Phys. Rev. Lett.* **1994**, *73*, 2107–2110.
- (56) Van der Ziel, A. *Solid State Physical Electronics*, 3rd ed.; Prentice-Hall Inc: Englewood Cliffs, NJ, 1976.
- (57) Drapak, S. I.; Kovalyuk, Z. D.; Netyaga, V. V.; Orletskii, V. B. *Tech. Phys. Lett.* **2002**, *28*, 707–710.
- (58) Fan, Z.; Fan, H.; Lu, Z.; Li, P.; Huang, Z.; Tian, G.; Yang, L.; Yao, J.; Chen, C.; Chen, D.; Yan, Z.; Lu, X.; Gao, X.; Liu, J.-M. *Phys. Rev. Appl.* **2017**, *7*, 014020.